

Galvanic molecular intercalation

Daniel Tezze¹, Covadonga Álvarez¹, Daniel Margineda¹, José Manuel Pereira¹, Umer Ahsan², Vlastimil Mazanek², Yogesh Kumar Maurya³, Aurelio Mateo-Alonso^{3,4}, Frederik M. Schiller^{5,6}, Fèlix Casanova^{1,4}, Samuel Mañas-Valero⁷, Eugenio Coronado⁷, Iván Rivilla^{4,6,8}, Zdenek Sofer², Beatriz Martín-García^{1,4}, Mainer Ormazá⁹, Luis E. Hueso^{1,4}, Marco Gobbi^{4,5*}

¹ CIC nanoGUNE BRTA, Donostia-San Sebastian, 20018, Spain

² Dept. of Inorganic Chemistry, University of Chemistry and Technology Prague, Technicka 5, 166 28 Prague 6, Czech Republic

³ POLYMAT, University of the Basque Country UPV/EHU San Sebastian, 20018, Spain

⁴ IKERBASQUE, Basque Foundation for Science, 48009 Bilbao, Spain

⁵ Materials Physics Center (CFM-MPC) Centro Mixto CSIC-UPV/EHU, San Sebastian, 20018, Spain

⁶ Donostia International Physics Center (DIPC), San Sebastián, 20018, Spain

⁷ Instituto de Ciencia Molecular (ICMol), Universitat de València, 46980 Paterna, Spain

⁸ Departamento de Química Orgánica I and Centro de Innovación y Química Avanzada (ORFEO-CINQA) Universidad del País Vasco (UPV/EHU), San Sebastian, 20018, Spain

⁹ Departamento de Polímeros y Materiales Avanzados: Física, Química y Tecnología, Facultad de Químicas (UPV/EHU), Apartado 1072, 20080, San Sebastián, Spain

*Corresponding authors:

marco.gobbi@ehu.eus

The intercalation of molecular species between the layers of van der Waals (vdW) materials has recently emerged as a powerful approach to combine the remarkable electronic and magnetic properties of vdW materials with the chemical flexibility of organic molecules¹⁻¹⁴. However, the full transformative potential of molecular intercalation remains underexplored, largely due to the lack of simple, broadly applicable methods that preserve high crystalline quality down to the few-layer limit.¹⁵⁻¹⁷ Here, we introduce a simple galvanic approach to intercalate different molecules into various vdW materials under ambient conditions, leveraging the low reduction potential of selected metals to enable a spontaneous molecular insertion. We employ our method, which is particularly well-suited for the in-situ intercalation of few-layer-thick crystals, to intercalate nine vdW materials, including magnets and superconductors, with molecules ranging from conventional alkylammonium ions to metallorganic and bio-inspired chiral cations. Notably, intercalation leads to a molecule-dependent enhancement of the superconducting transition in 2H-TaS₂, reaching a critical temperature of 4.7 K, higher than TaS₂ monolayers.¹⁸ Additionally, α -RuCl₃ exhibits an unprecedented transition from antiferromagnetic to ferrimagnetic ordering upon intercalation with cobaltocenium. These results establish our approach as a versatile technique for engineering atomically thin quantum materials and heterostructures, unlocking the transformative effects of molecular intercalation.

The intercalation of guest molecules in a host vdW material is typically achieved through a chemical or an electrochemical approach^{1,9,10,14,19-21}. In solution-based chemical intercalation strategies, a vdW material is treated in a solvent containing a molecular species which spontaneously occupies the vdW gap^{22,23}. However, this method is constrained by the requirement of a specific alignment between the frontier energy levels of host and guest, greatly limiting the choice of vdW materials and molecules^{23,24}. Besides, harsh conditions such as high temperature, pressure, or extended reaction time are required, which may compromise the material integrity, in particular when few-nm-thick crystals are processed^{25,26}. Electrochemical intercalation employs an external potential to trigger the intercalation process in a broader class of vdW

materials^{10,16,21,24,27}. Despite its versatility, the out-of-equilibrium nature of this method makes it inherently aggressive and difficult to control,^{28,29} often yielding intercalated compounds with lower structural quality than pristine materials.^{29,30} While traditionally used for bulk crystals²⁹⁻³⁴, electrochemical intercalation has recently been adapted for few-nm-thick flakes contacted by micrometric electrodes^{15-17,35}. However, this in-situ intercalation requires a complex device fabrication and a highly controlled environment to minimize side reactions, host material exfoliation and degradation of electrical contacts^{16,17}.

Here, we present a simple galvanic intercalation process which is particularly well-suited for intercalating few-nm-thick flakes of different materials with molecular cations (**Figure 1a**). In this method, a vdW host (vdWh) material is electrically connected to a metal (M) with a low reduction potential, such as In⁰, Zn⁰ or Mg⁰. For example, the host crystal can be a flake transferred onto a gold-coated substrate, electrically in contact with In⁰. Then, both vdW and M are immersed in a non-aqueous solution containing a salt of the target molecular guest (G⁺). Under these conditions, and for certain combination of vdW, M and G⁺, the system behaves as a galvanic cell. The low-reduction-potential M acts as the anode, undergoing spontaneous oxidation ($M^0 \rightarrow M^{x+} + xe^-$, $x = 1, 2, 3, \dots$). The vdWh serves as the cathode, being electrochemically reduced by electrons provided by the metal oxidation through the electrical connection ($vdWh + e^- \rightarrow vdWh^-$). To preserve charge neutrality within the vdW material, molecular ions are introduced into the vdW gap, leading to the intercalation ($vdWh^- + G^+ \rightarrow G-vdWh$). This intercalation mechanism implies that for each G⁺ introduced in the vdW gap, an electron is formally introduced in the band structure of the vdWh, leading to a large charge carrier doping (on the order of 10¹⁴ charges/cm² in each layer).¹¹ While an analogous approach was employed to intercalate different vdW compounds with alkali and alkaline earth metals (e.g. Li⁺)³⁶⁻⁴⁰, it has not been explored to achieve molecular intercalation. We highlight that the whole process can be carried out in air, as In⁰, Zn⁰ or Mg⁰ are stable and can be handled in air.

Figure 1b illustrates how the galvanic approach offers a different reaction path as compared to chemical intercalation. Our approach makes the process spontaneous for certain host-guest pairs

which cannot be chemically intercalated for thermodynamic reasons (*Path 1* \rightarrow *Path 1**), and accelerates it for other materials where chemical intercalation is slow (*Path 2* \rightarrow *Path 2**), eliminating the need for high temperatures and/or long intercalation times.

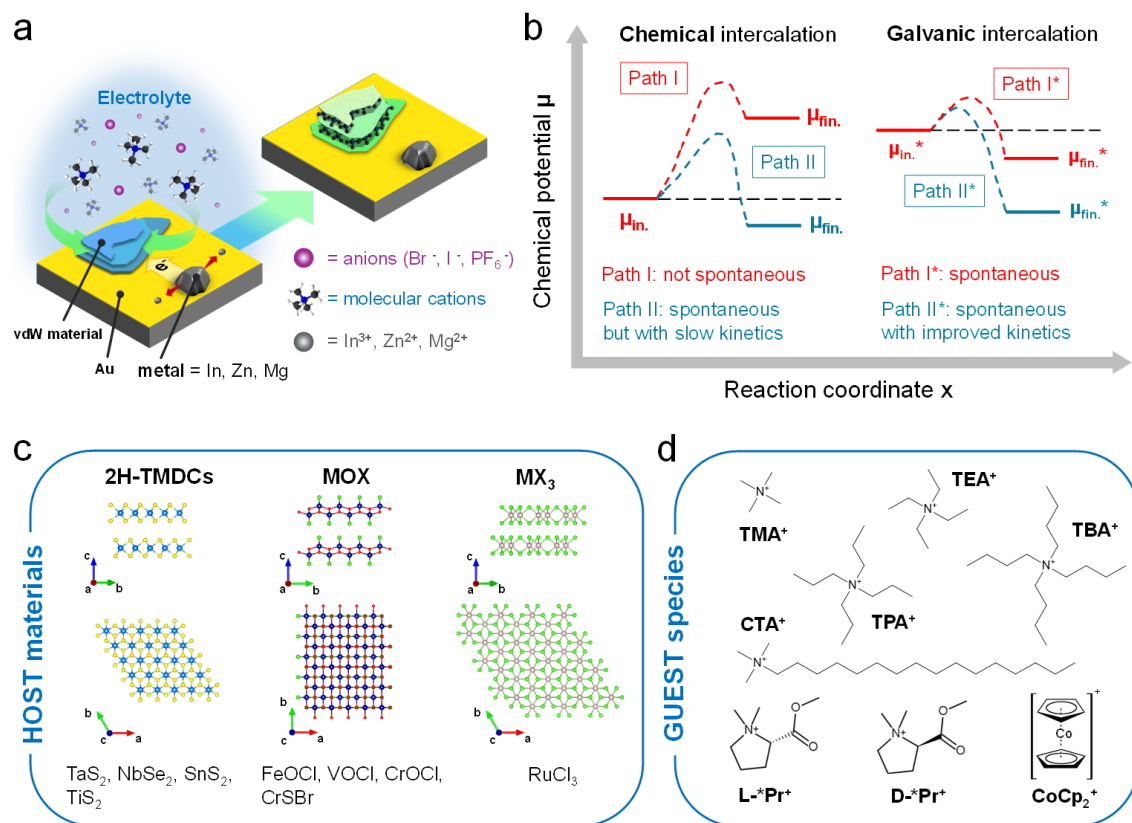


Figure 1. Concept of Galvanic Intercalation: (a) Sketch of a galvanic cell for intercalating a vdW crystal, such as a flake (cathode) with molecular cations, using a suitable metal (In⁰, Zn⁰, Mg⁰) as the anode. The sketch depicts a flake exfoliated on a Au-coated substrate as a target crystal, and an In⁰ piece as anodic metal. When the substrate is immersed in a solution, spontaneous half-reactions generate an in-built electrical potential that drives the molecular intercalation. (b) *Left* – Schematic of chemical potential profiles showing a generic non-spontaneous (*path 1*) and a spontaneous, yet kinetically hindered (*path 2*) chemical intercalation pathway between two states, μ_{in} . (reagents) and μ_{fin} . (products). *Right* – Galvanic intercalation provides alternative reaction pathways, making a previously non-spontaneous reaction spontaneous (*path 1**) or improving intercalation kinetics (*path 2**). (c) Layered vdW materials successfully intercalated via galvanic intercalation. (d) Molecular cations chosen as guest species for the hybrid superlattices in this work: alkylammonium ions (TMA⁺, TEA⁺, TPA⁺, TBA⁺, and CTA⁺), the two enantiomers of a prolinium derivative (L-*Pr⁺ and D-*Pr⁺), and the organometallic cobaltocenium ion (CoCp₂⁺).

The families of vdW compounds which we successfully intercalated using the galvanic approach include superconducting transition metal dichalcogenides, magnetic metal oxyhalides and trihalides (**Figure 1 c**). Notably, most of these materials can be chemically intercalated with Lewis bases^{23,41}, whereas the intercalation of cations typically requires a more demanding electrochemical approach. As guest molecular cations, we focused on common alkylammonium ions that differ in size and shape (TMA⁺, TEA⁺, TPA⁺, TBA⁺, CTA⁺), a chiral prolinium-derivative (left-hand L-*Pr⁺ and right-handed D-*Pr⁺) and cobaltocenium (CoCp₂⁺), as depicted in **Figure 1d**. We successfully intercalated at least two of these molecules into each of the nine different vdW compounds tested, achieving a total of 49 organic-inorganic superlattices (**Supplementary Table 1**). Our method is versatile and adaptable for intercalating bulk crystals and multiple exfoliated flakes on a conductive substrate or an individual few-nm-thick flake.

Figure 2 shows how galvanic intercalation yields novel magnetic and superconducting metamaterials. Specifically, we employed an experimental setup as the one shown in **Figure 2a** to intercalate bulk crystals of α -RuCl₃, with CoCp₂⁺ ions and 2H-TaS₂ with TMA⁺ ions. The galvanic intercalation process is accompanied by a spontaneous current at zero applied voltage, generated by the in-built electrical potential between the short-circuited cathode and the anode, which can be measured by an amperemeter connected to the external wire. **Figure 2b** shows the evolution of the galvanic current over time for the intercalation of α -RuCl₃ with CoCp₂⁺ ions. Based on this data, we estimated the stoichiometric index $x = 0.27 \pm 0.01$ for (CoCp₂)_xRuCl₃, averaging over different crystals (**Supplementary Table 2**).

The intercalation of RuCl₃ with Co(Cp)₂⁺ was confirmed by X-Ray diffraction (XRD). This technique enables a comprehensive assessment of the intercalation process, as it provides a precise measurement of the interlayer distance, which is dramatically altered by the insertion of molecular guests. Moreover, the full width at half maximum (FWHM) of the diffraction peaks provides an indication of crystalline quality. In **Figure 2c** we compare the XRD patterns of a bulk α -RuCl₃ crystal measured before and after galvanic intercalation. After intercalation, the XRD pattern of the crystal exhibits one set of very sharp (00l) peaks shifted to lower angles compared

to the pristine material, indicating an increase in interlayer distance from 5.7(4) Å to 10.9(3) Å ($\Delta d = 5.19$ Å). The pristine and intercalated crystals display diffraction peaks with similar FWHM, revealing almost unaffected crystalline quality. X-ray photoelectron spectroscopy revealed the reduction of a fraction of Ru(III) to Ru(II) in α -RuCl₃, as a consequence of the charge transfer induced by intercalation (**Supplementary Figure 1**).

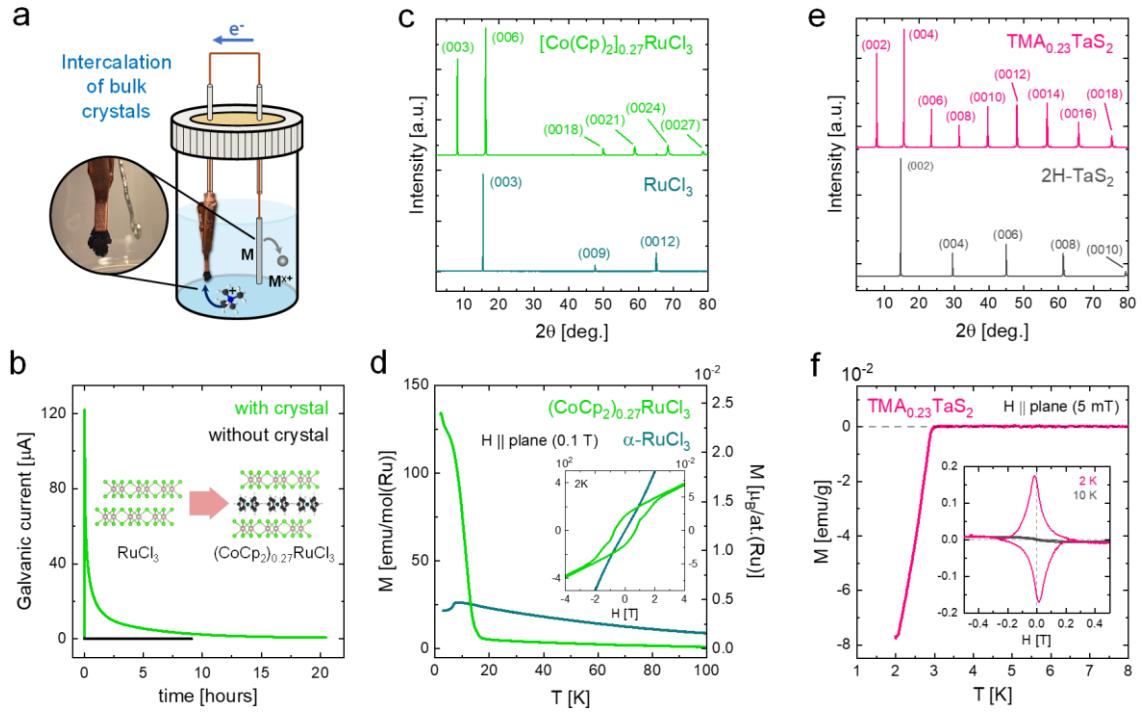


Figure 2. Tuning magnetism and superconductivity in bulk crystals through galvanic molecular intercalation: (a) Experimental setup for the galvanic molecular intercalation process of bulk crystals. (b) Galvanic current over time recorded at zero applied voltage during the intercalation of a α -RuCl₃ crystal ($m_p = 2.66$ mg) with Co(Cp)₂⁺ ions, using a 10 mM CoCp₂PF₆/ACN electrolyte (30 mL). (c) X-ray diffraction pattern acquired for a pristine α -RuCl₃ crystal and after the intercalation process with CoCp₂⁺ ions. (d) Temperature dependence of the in-plane magnetization, M(T), of a pristine α -RuCl₃ crystal and a (CoCp₂)_{0.27}RuCl₃ crystal, recorded at H = 0.1 T. *Inset*: in-plane hysteresis loop recorded at 2K for pristine α -RuCl₃ crystal and (CoCp₂)_{0.27}RuCl₃ crystal. (e) X-ray diffraction pattern measured for a pristine 2H-TaS₂ crystal and after intercalation with TMA⁺ ions, using a 5 mM TMAB/MeOH electrolyte. (f) In-plane zero-field-cooled (ZFC) magnetization over temperature, M(T), of pristine and TMA_{0.23}TaS₂, recorded at H = 5 mT. *Inset*: Field dependence of the magnetization of TMA_{0.23}TaS₂ recorded at 2 K and 10 K.

The magnetic properties are also dramatically changed by intercalation. While pristine α -RuCl₃ exhibits antiferromagnetic behavior with a Neel temperature of ~ 7 K⁴², (CoCp₂)_{0.27}RuCl₃ shows a spontaneous magnetization below ~ 13 K (**Figure 2d**). At 2 K, (CoCp₂)_{0.27}RuCl₃ displays a magnetic hysteresis characterized by a finite remanence and a large coercivity ($H_c \sim 7.0$ kOe, inset in **Figure 2d**). Additional magnetic characterization of pristine and CoCp₂⁺ intercalated α -RuCl₃ is presented in **Supplementary Figure 2**. Based on this magnetic characterization, we conclude that (CoCp₂)_{0.27}RuCl₃ is a ferrimagnetic compound with in-plane anisotropy and enhanced transition temperature. Notably, long-range magnetic ordering was not observed in α -RuCl₃ intercalated with TMA⁺ ions in a previous study⁴³, indicating an active role of the metallorganic CoCp₂⁺ ions in the emergent magnetization, in agreement with recent works on CoCp₂-intercalated 2H-SnS₂⁶ and 2H-SnSe₂⁷.

Next, we focus on the effect of intercalation of TMA⁺ on 2H-TaS₂, which is a superconductor with $T_c \sim 0.8$ K in its pristine state.¹⁸ XRD confirms the successful generation of a high-quality hybrid superlattice (**Figure 2e**). To characterize the superconductive nature of the intercalated crystal, we measured the temperature dependence of the zero-field-cooled magnetization (**Figure 2f**). The negative magnetization recorded below 2.95 K, signature of the Meissner effect, indicates the formation of superconducting correlation at an enhanced T_c . The magnetic field dependence of the magnetization measured at 2K presents a hysteresis, indicating that TMA-TaS₂ is a type-II superconductor (inset in **Figure 2f**)⁴⁴⁻⁴⁶. A similar enhancement of T_c has been observed for chemically and electrochemically intercalated TaS₂ crystals, which however often present much lower crystallinity, poor sample integrity and limited thermal stability.^{25,26,47} X-ray fluorescence measurements performed on galvanically intercalated α -RuCl₃ and 2H-TaS₂ bulk crystals detected no traces of Zn and In (**Supplementary Figure 3**), while residual of the solvents are present in the intercalated compounds (see **Supplementary Table 2**).

The galvanic approach is compatible with the intercalation of randomly distributed flakes transferred on a conducting substrate (see **Figure 3a** and Methods). In this case, the anodic metal is electrically connected to the substrate, and both are immersed in a solution of the chosen

molecular salt. This procedure is straightforward and closely resembles chemical intercalation, except for the presence of the anodic metal in electrical contact with the flakes.

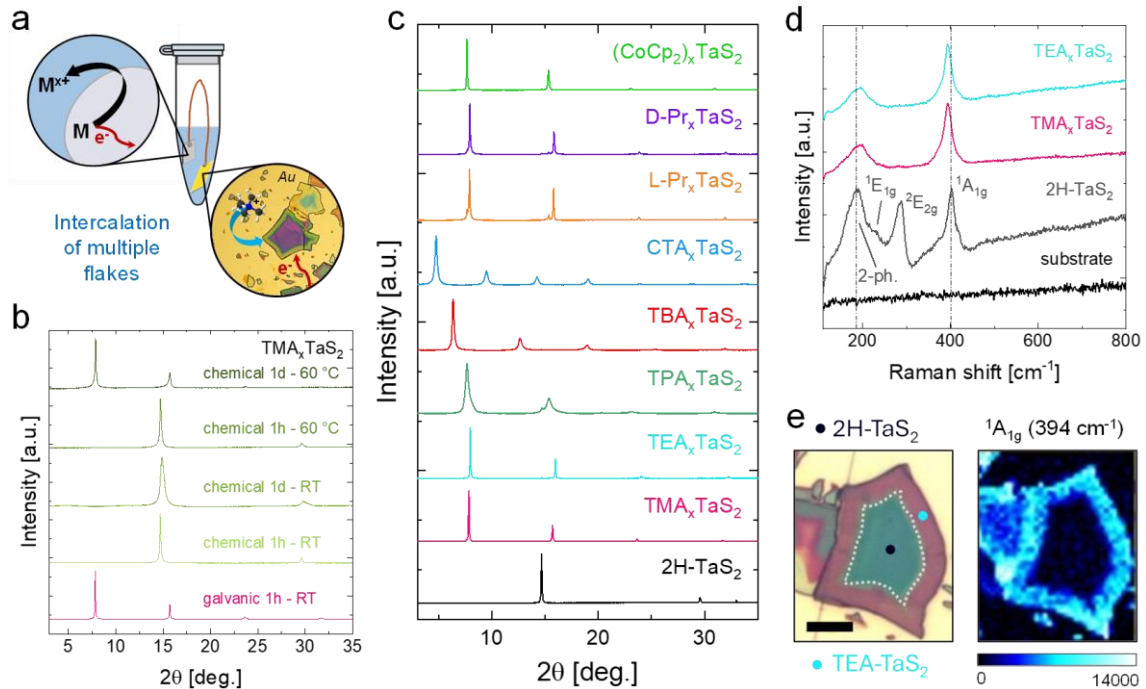


Figure 3. Galvanic molecular intercalation of different molecules in multiple exfoliated flakes: (a) Scheme of the setup used for the galvanic intercalation of multiple flakes exfoliated and transferred onto an Au thin film coated SiO₂ substrate. **(b)** Comparison between the XRD patterns measured for 2H-TaS₂ flakes intercalated with TMA⁺ using either the galvanic or the conventional chemical approach (at different conditions). **(c)** X-ray diffraction patterns measured for multiple pristine and intercalated 2H-TaS₂ exfoliated flakes, with all the eight molecular ions (G⁺) considered in this work. **(d)** Micro-Raman spectra measured for pristine 2H-TaS₂ and TMA⁺ and TEA⁺ intercalated 2H-TaS₂ flakes. **(e)** Optical image (*left*) and Raman map (*right*) of the intensity of the 1A_{1g} mode of a 2H-TaS₂ flake partially intercalated with TEA⁺ ions.

To compare the two approaches, we present the XRD patterns of 2H-TaS₂ intercalated with TMA⁺ using either the chemical or the galvanic method (**Figure 3b**). Whereas a successful intercalation is achieved after 1h at room temperature using the galvanic method, chemical intercalation requires significantly higher temperatures (60 °C in MeOH) and a much longer duration (~ 1 day) to be effective. Notably, the galvanic approach exhibits higher crystalline quality, as indicated by the narrower XRD peaks.

Given the simplicity and efficiency of the galvanic intercalation of flakes, we used this method to systematically evaluate the compatibility of various vdW materials and molecules for generating a library of hybrid superlattices. All the molecules displayed in **Figure 1d** were successfully intercalated in 2H-TaS₂ (**Figure 3c**), FeOCl and α -RuCl₃, as confirmed by XRD measurements (**Supplementary Figures 4-6**). Moreover, other six vdW compounds could be intercalated with at least two molecules (**Supplementary Figures 7-12**). All intercalated compounds display high crystalline quality, as indicated by the sharp and well-defined XRD peaks. Additionally, we tested an ion-exchange approach to substitute TMA⁺ with CoCp₂⁺ ions²⁹ in galvanically pre-intercalated 2H-SnS₂ and CrOCl, further increasing the number of guest molecules compatible with our approach (**Supplementary Figure 13**).

Raman spectroscopy is a powerful tool to characterize the intercalation at the single-flake level, as the phonon modes are profoundly modified by intercalation. As an example, we focus on TaS₂. The Raman spectrum of pristine 2H-TaS₂ presents three characteristic peaks, corresponding to the 2-phonon (186 cm⁻¹), E_{2g} (286 cm⁻¹), and A_{1g} (402 cm⁻¹) modes (**Figure 3d**). In the TMA- and TEA-TaS₂ flakes the ¹A_{1g} peak shifts considerably to 394 cm⁻¹, the two-phonon mode slightly moves to higher wavenumbers, and the ²E_{2g} peak is totally suppressed. Additionally, the intensity of all peaks is increased after intercalation. This is evident in **Figure 3d**, as the signal to noise ratio is markedly higher for the intercalates than for the pristine, even if the spectrum of the pristine was recorded with higher laser power. These changes are observed in 2H-TaS₂ flakes intercalated also with TPA⁺, TBA⁺ and CTA⁺ ions (**Supplementary figure 14**). Notably, the Raman spectroscopy characterization also confirms that the galvanic process is also successful for intercalating ultrathin flakes, which can be occasionally found on the substrate, but do not contribute significantly to the diffracted intensity of X-rays (**Supplementary Figure 14**).

Intercalation is a topotactic process⁴⁸ proceeding from the flake's perimeter towards the center with a progressing front, often visible at optical microscope or TEM^{38,49}. For some molecules, such as TEA⁺ and CoCp₂⁺, there is a defined intercalation front and the process is sufficiently slow that can be interrupted before completion. This yields partially intercalated flakes with a

relative sharp boundary between pristine and intercalated regions ($< 0.5 \mu\text{m}$). **Figure 3e** shows a representative optical image of one of these flakes, which was intercalated with TEA^+ ions for 1 hour using In^0 as the anode. A map of the ${}^1\text{A}_{1g}$ peak intensity shows a clear enhancement of the Raman signal in the region close to the flake's edge, confirming the partial intercalation and the presence of a sharp interface between the pristine and intercalated phases. This spatially controlled intercalation offers the possibility to define lateral heterostructures with different physical properties within the same flake, a key requirement for fabricating advanced electronic devices.

Finally, we demonstrate that galvanic molecular intercalation can also be successfully performed on preselected individual flakes integrated in a device, which represents an ideal testbed for measuring transport properties. To explore this approach, we have focused on superconducting 2H-TaS_2 and 2H-NbSe_2 , characterizing the evolution of their electrical properties following the intercalation of different molecules. Intercalating single flakes involves transferring the target flake onto pre-patterned metallic electrodes, connecting the anodic metal to one of the electrodes, and covering the device with a drop of the solution of the target molecular salt, which closes the circuit of the galvanic cell-on-a-chip (**Figure 4a**). The homogeneous intercalation of the flake, which changes color during intercalation, is confirmed by Raman spectroscopy (**Supplementary Video 1 and Supplementary Figure 15**).

This single-flake intercalation also provides additional experimental evidence of the efficiency of the galvanic approach. **Figure 4b** shows an area of the substrate with an Au electrode connected to an In piece and two 2H-TaS_2 flakes fortuitously close to each other, with only one in contact with Au. After applying a drop of the target electrolyte, a clear color change is observed for the flake touching the Au electrode, but not for the other, indicating that only the flake electrically connected to In is effectively intercalated. This highlights the potential of galvanic intercalation to selectively intercalate target crystals.

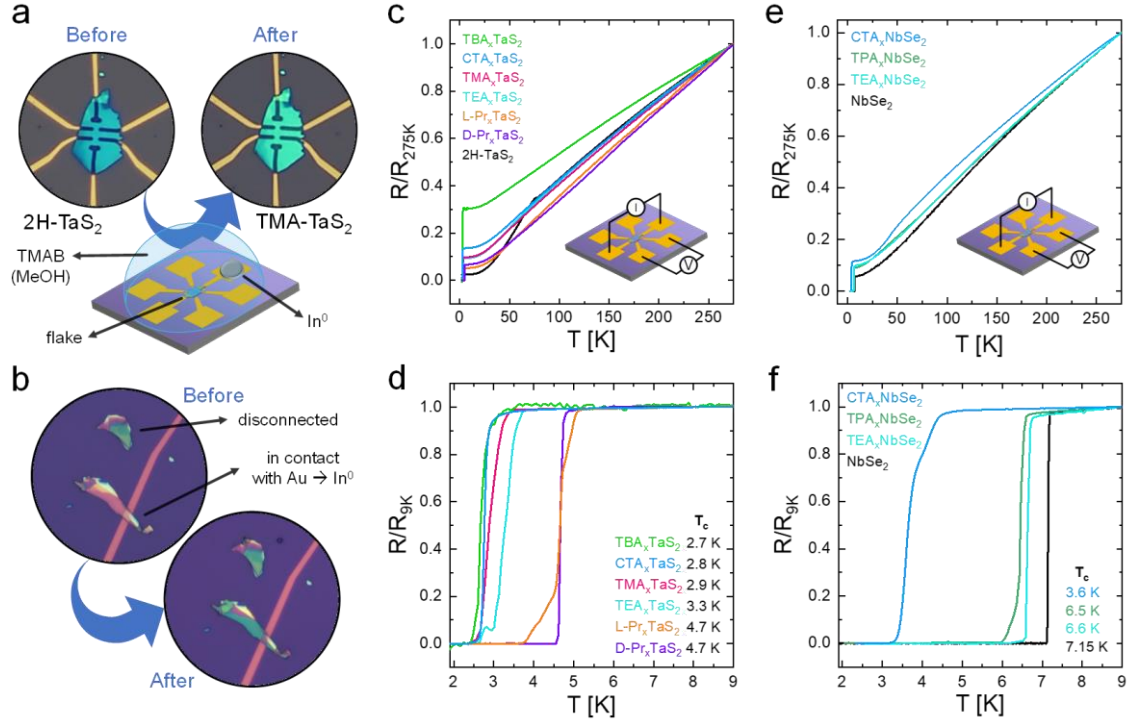


Figure 4. Galvanic molecular intercalation of different molecules in single-flake devices: (a) Optical image of a single flake of 2H-TaS₂ stamped on SiO₂/Si substrate with pre-patterned Au contacts before (left) and after (right) the intercalation process. The color change, due to the change in the thickness of the flake, is the first indication of intercalation success. (b) Optical images of two flakes acquired before and after adding a drop of the electrolyte onto the substrate. One flake touches the Au electrode connected to the In⁰ as the anode, and one is separated from it. Only the flake connected to the In⁰ as the anode through the Au electrode is intercalated, as confirmed by the color change. (c-d) Temperature dependence of the resistance of 2H-TaS₂ flakes intercalated with the different molecules in the ranges 1.9 K – 275 K and 1.9 K – 9 K. (e-f) Temperature dependence of the resistance of 2H-NbSe₂ flakes intercalated with the different molecules in the ranges 1.9 K – 275 K and 1.9 K – 9 K. In (c) and (e), the resistance is normalized to the resistance value at 275 K; in (d) and (f), it is normalized to the resistance value at 9 K.

Next, we focus on the superconducting tunability of different vdWhs. **Figure 4c** shows the temperature dependence of the resistance $R(T)$ of 2H-TaS₂ intercalated with six different organic cations in the temperature range 1.9 K – 275 K. In all cases, a metallic behavior is recorded after intercalation. At low temperatures, all intercalates exhibit a transition to a superconducting state (**Figure 4d**). The transition is remarkably sharp in the context of organic-intercalated vdWh materials, with the derivative of the $R(T)$ trace displaying a FWHM between 0.1 K and 0.2 K,

indicating a highly homogeneous superconducting state. We note that pristine 2H-TaS₂ flakes with a number of layers comparable to that used in this experiment have a critical temperature T_c of approximately 0.8 K,¹⁸ not accessible in our setup. Therefore, the galvanic intercalation of the molecular guests leads to a pronounced enhancement of T_c in the few-layer-thick flakes. Notably, the modification of the superconducting state is guest-dependent. For instance, the intercalation of TMA⁺, TEA⁺, TBA⁺ and CTA⁺, which are chemically similar alkylammonium cations but in different sizes, results in T_c values between 2.7 K and 3.3 K. These T_c are higher than that of bulk 2H-TaS₂ crystal and comparable to 1H-TaS₂ monolayer's, suggesting that these alkylammonium compounds act as spacers, increasing the interlayer separation in TaS₂, and providing monolayer behavior to the few-nm-thick flakes. Remarkably, a T_c of 4.7 K is recorded for both L/D-*Pr⁺-TaS₂ intercalates, higher than that of 2H-TaS₂ monolayer¹⁸ and close to the highest T_c reported for molecule-intercalated 2H-TaS₂^{26,47}. Beside the alkylammonium moiety, L/D-*Pr⁺ possesses a polar C=O group, which may hybridize or interact with dipolar interaction with 2H-TaS₂, possibly being responsible for the anomalously high T_c. Moreover, prolinium-derivatives intercalation is also particularly intriguing, as it is a chiral molecule, which may provide peculiar spin transport properties and unconventional superconductivity^{4,5}. Overall, our data indicates that the T_c of 2H-TaS₂ is not only influenced by the interlayer distance or doping level, but also by the chemical nature of the guest species.

The behavior of 2H-NbSe₂ intercalated flakes is shown in **Figure 4e - f**. The molecular intercalation decreases T_c from 7.1 K, characteristic of bulk 2H-NbSe₂, to a value that depends on the alkylammonium ion chosen as guest species (**Figure 1d**). Unlike 2H-TaS₂, T_c in 2H-NbSe₂ monotonically decreases with the number of layers (starting from 7-8 layers), compared to the bulk value. Therefore, the decrease in T_c following the intercalation is consistent with monolayer behavior in few layer flakes. In particular, CTA-NbSe₂ displays the lowest T_c and the highest interlayer distance (15.0 Å) among the NbSe₂ intercalates.^{28,31,50}

Our results demonstrate that galvanic molecular intercalation is a versatile and effective method to incorporate diverse molecular cations into a wide range of vdW materials, from bulk crystals

to individual few-layers flakes. The numerous materials synthesized in this study, many of which remain to be fully characterized in detail, are anticipated to exhibit novel magnetic and superconductive properties. Tuning intercalation conditions – such as testing different electrolytes, anodic metals, concentrations, and temperatures – will expand the applicability of the galvanic approach to a broader range of host-guest combinations. Additionally, our approach enables the creation of lateral heterostructures between intercalated and pristine regions in the same crystal. It also allows for the selective intercalation of target flakes integrated in vdW heterostructures, potentially unlocking new functionalities in vdW materials and devices.

Data availability

All data in the main text or Supplementary Information are available from the corresponding authors on reasonable request.

References

1. Wan, Z., Qian, Q., Huang, Y. & Duan, X. Layered hybrid superlattices as designable quantum solids. *Nature* **635**, 49–60 (2024).
2. Coronado, E. *et al.* Hybrid Magnetic/Superconducting Materials Obtained by Insertion of a Single-Molecule Magnet into TaS₂ Layers. *Advanced Materials* **23**, 5021–5026 (2011).
3. Bian, Z. *et al.* Chiral Van Der Waals Superlattices for Enhanced Spin-Selective Transport and Spin-Dependent Electrocatalytic Performance. *Advanced Materials* **35**, 2306061 (2023).
4. Qian, Q. *et al.* Chiral molecular intercalation superlattices. *Nature* **606**, 902–908 (2022).
5. Wan, Z. *et al.* Unconventional superconductivity in chiral molecule–TaS₂ hybrid superlattices. *Nature* **632**, 69–74 (2024).
6. Liu, Y. *et al.* Room-temperature long-range ferromagnetic order in a confined molecular monolayer. *Nat. Phys.* **20**, 281–286 (2024).
7. Liu, Y. *et al.* Interfacial Charge-Transfer Excitonic Insulator in a Two-Dimensional Organic–Inorganic Superlattice. *J. Am. Chem. Soc.* **146**, 21044–21051 (2024).

8. Stark, M. S., Kuntz, K. L., Martens, S. J. & Warren, S. C. Intercalation of Layered Materials from Bulk to 2D. *Advanced Materials* **31**, 1808213 (2019).
9. Zhou, J. *et al.* Layered Intercalation Materials. *Advanced Materials* **33**, 2004557 (2021).
10. Rajapakse, M. *et al.* Intercalation as a versatile tool for fabrication, property tuning, and phase transitions in 2D materials. *npj 2D Mater Appl* **5**, 30 (2021).
11. Wu, Y., Li, D., Wu, C.-L., Hwang, H. Y. & Cui, Y. Electrostatic gating and intercalation in 2D materials. *Nat Rev Mater* **8**, 41–53 (2022).
12. Pereira, J. M., Tezze, D., Ormaza, M., Hueso, L. E. & Gobbi, M. Engineering Magnetism and Superconductivity in van der Waals Materials via Organic-Ion Intercalation. *Advanced Physics Research* **2**, 2200084 (2023).
13. Li, M., Fan, Q., Gao, L., Liang, K. & Huang, Q. Chemical Intercalation of Layered Materials: From Structure Tailoring to Applications. *Advanced Materials* 2312918 (2024) doi:10.1002/adma.202312918.
14. Zhou, J. *et al.* Modular assembly of a library of hybrid superlattices and artificial quantum solids. *Matter* **7**, 1131–1145 (2024).
15. Bediako, D. K. *et al.* Heterointerface effects in the electrointercalation of van der Waals heterostructures. *Nature* **558**, 425–429 (2018).
16. Wang, C. *et al.* Monolayer atomic crystal molecular superlattices. *Nature* **555**, 231–236 (2018).
17. He, Q. *et al.* In Situ Probing Molecular Intercalation in Two-Dimensional Layered Semiconductors. *Nano Lett.* **19**, 6819–6826 (2019).
18. Yang, Y. *et al.* Enhanced superconductivity upon weakening of charge density wave transport in 2H-TaS₂ in the two-dimensional limit. *Phys. Rev. B* **98**, 035203 (2018).
19. Li, Z. *et al.* Intercalation Strategy in 2D Materials for Electronics and Optoelectronics. *Small Methods* **5**, 2100567 (2021).
20. Wang, Z., Li, R., Su, C. & Loh, K. P. Intercalated phases of transition metal dichalcogenides. *SmartMat* **1**, e1013 (2020).

21. Zhang, Q., Mei, L., Cao, X., Tang, Y. & Zeng, Z. Intercalation and exfoliation chemistries of transition metal dichalcogenides. *J. Mater. Chem. A* **8**, 15417–15444 (2020).
22. Stanley Whittingham, M. Intercalation Chemistry: An Introduction. in *Intercalation Chemistry* 1–18 (Elsevier, 1982). doi:10.1016/B978-0-12-747380-2.50006-7.
23. Jacobson, A. J. Organic and Organometallic Intercalation Compounds of the Transition Metal Dichalcogenides. in *Intercalation Chemistry* 229–265 (Elsevier, 1982). doi:10.1016/B978-0-12-747380-2.50012-2.
24. Jeong, S. *et al.* Tandem intercalation strategy for single-layer nanosheets as an effective alternative to conventional exfoliation processes. *Nat Commun* **6**, 5763 (2015).
25. Pereira, J. M. *et al.* Enhanced Superconductivity in 2H-TaS₂ Devices through in Situ Molecular Intercalation. *ACS Appl. Mater. Interfaces* **16**, 41626–41632 (2024).
26. Gamble, F. R. *et al.* Intercalation Complexes of Lewis Bases and Layered Sulfides: A Large Class of New Superconductors. *Science* **174**, 493–497 (1971).
27. Wang, S. *et al.* Electrochemical molecular intercalation and exfoliation of solution-processable two-dimensional crystals. *Nat Protoc* **18**, 2814–2837 (2023).
28. Yu, L. *et al.* Intercalation-Induced Monolayer Behavior in Bulk NbSe₂. *ACS Appl. Mater. Interfaces* **16**, 59049–59055 (2024).
29. Tezze, D. *et al.* Tuning the magnetic properties of NiPS₃ through organic-ion intercalation. *Nanoscale* **14**, 1165–1173 (2022).
30. Pereira, J. M. *et al.* Percolating Superconductivity in Air-Stable Organic-Ion Intercalated MoS₂. *Adv Funct Materials* **32**, 2208761 (2022).
31. Zhang, H. *et al.* Tailored Ising superconductivity in intercalated bulk NbSe₂. *Nat. Phys.* **18**, 1425–1430 (2022).
32. Zhang, H. *et al.* Enhancement of superconductivity in organic-inorganic hybrid topological materials. *Science Bulletin* **65**, 188–193 (2020).
33. Wang, N. *et al.* Transition from Ferromagnetic Semiconductor to Ferromagnetic Metal with Enhanced Curie Temperature in Cr₂Ge₂Te₆ via Organic Ion Intercalation. *J. Am. Chem. Soc.* **141**, 17166–17173 (2019).

34. Rendenbach, B., Hohl, T., Harm, S., Hoch, C. & Johrendt, D. Electrochemical Synthesis and Crystal Structure of the Organic Ion Intercalated Superconductor $(TMA)_{0.5}Fe_2Se_2$ with $T_c = 43$ K. *J. Am. Chem. Soc.* **143**, 3043–3048 (2021).
35. Zhang, J. *et al.* Reversible and selective ion intercalation through the top surface of few-layer MoS₂. *Nat Commun* **9**, 5289 (2018).
36. Ji, K. *et al.* Lithium intercalation into bilayer graphene. *Nat Commun* **10**, 275 (2019).
37. Li, Y., Lu, Y., Adelhelm, P., Titirici, M.-M. & Hu, Y.-S. Intercalation chemistry of graphite: alkali metal ions and beyond. *Chem. Soc. Rev.* **48**, 4655–4687 (2019).
38. Xiong, F. *et al.* Li Intercalation in MoS₂: In Situ Observation of Its Dynamics and Tuning Optical and Electrical Properties. *Nano Lett.* **15**, 6777–6784 (2015).
39. Whittingham, M. S. & Gamble, F. R. The lithium intercalates of the transition metal dichalcogenides. *Materials Research Bulletin* **10**, 363–371 (1975).
40. Roy, A. *et al.* Improving rechargeable magnesium batteries through dual cation co-intercalation strategy. *Nat Commun* **15**, 492 (2024).
41. Dines, M. B. Intercalation of Metallocenes in the Layered Transition-Metal Dichalcogenides. *Science* **188**, 1210–1211 (1975).
42. Wagner, J. *et al.* Magneto-optical study of metamagnetic transitions in the antiferromagnetic phase of α -RuCl₃. *npj Quantum Mater.* **7**, 28 (2022).
43. Jo, M. *et al.* Enhancement of Photoresponse on Narrow-Bandgap Mott Insulator α -RuCl₃ via Intercalation. *ACS Nano* **15**, 18113–18124 (2021).
44. Inhaber, H. Magnetic hysteresis in type II superconductors. *Solid State Communications* **11**, 535–538 (1972).
45. Lai, X. *et al.* Observation of Superconductivity in Tetragonal FeS. *J. Am. Chem. Soc.* **137**, 10148–10151 (2015).
46. Pan, J. *et al.* Enhanced Superconductivity in Restacked TaS₂ Nanosheets. *J. Am. Chem. Soc.* **139**, 4623–4626 (2017).

47. Hauptmann, A., Lerf, A. & Biberacher, W. Intercalation Compounds of Large Organic Molecular Cations in the Layered Dichalcogenide 2H-TaS₂. *Zeitschrift für Naturforschung B* **51**, 1571–1575 (1996).
48. Cahen, S., Speyer, L., Lagrange, P. & Hérold, C. Topotactic Mechanisms Related to the Graphene Planes: Chemical Intercalation of Electron Donors into Graphite. *Eur J Inorg Chem* **2019**, 4798–4806 (2019).
49. Yoshida, K., Kawasaki, T., Kuwabara, A., Ukyo, Y. & Ikuhara, Y. In situ electron microscopic observation of electrochemical Li-intercalation into MoS₂. *Solid State Ionics* **357**, 115488 (2020).
50. Scheidt, E.-W. *et al.* On the nature of superconductivity in the anisotropic dichalcogenide NbSe₂ {CoCp₂}_x. *J. Phys.: Condens. Matter* **27**, 155701 (2015).
51. Boix-Constant, C. *et al.* Probing the Spin Dimensionality in Single-Layer CrSBr Van Der Waals Heterostructures by Magneto-Transport Measurements. *Advanced Materials* **34**, 2204940 (2022).
52. Bockman, T. M. & Kochi, J. K. Charge-transfer ion pairs. Structure and photoinduced electron transfer of carbonylmetalate salts. *J. Am. Chem. Soc.* **111**, 4669–4683 (1989).

Experimental section

Materials: *Van der Waals crystals* – 2H-TaS₂ crystals were purchased from HQ Graphene. 2H-NbSe₂, 2H-TiS₂, 2H-SnS₂, FeOCl, VOCl, CrOCl, α -RuCl₃ crystals were made by chemical vapor transport (CVT). Synthesis protocols are reported in **Supplementary Methods 1**. CrSBr crystals were synthesized by CVT and characterized by powder and crystal X-ray diffraction, energy dispersive X-ray analysis, high-resolution transmission electron microscopy, superconducting quantum interference device magnetometry and temperature-dependent single crystal diffraction, as reported previously⁵¹.

Anodic metals – Indium wire (purity 99.99 %) was purchased from CMR-Direct, Zinc (purity 99.9%) were purchased from G. L. Y. (by Amazon S.p.A.) and Magnesium (purity 99.95%) from S. X. Keji Co. Ltd (by Amazon S.p.A.). Platinum plates were obtained by pressing metallic pellets (purity 99.99%, Kurt J. Lesker). Before any usage, Zn⁰ and Mg⁰ plates are polished with sandpaper and rinsed with iso-propanol. Platinum plates are polished with sandpaper and sonicated for two minutes in acetone and then in isopropanol for surface cleaning.

Organic Salts – Tetramethylammonium bromide (TMAB, purity \geq 98 %), tetraethylammonium bromide (TEAB, purity = 98%), tetrapropylammonium bromide (TPAB, purity = 98 %), tetrabutylammonium bromide (TBAB, purity \geq 98 %), bis-(cyclopentadienyl)cobalt(III) hexafluorophosphate (Co(Cp)₂PF₆, purity 98%) and cetyltrimethylammonium bromide (CTAB, purity \geq 99%) was purchased from Across Organics. Before usage, salts were dehydrated at 100° C in vacuum (~ 1 mbar) overnight, except for Bis(cyclopentadienyl)cobalt(III) iodide (CoCp₂I) and (S)- and (R)-2-(methoxycarbonyl)-1,1-dimethylpyrrolidin-1-ium iodide (L-*PrI and D-*PrI), which were only vacuum dried (~ 1 mbar) overnight after their synthesis.

CoCp₂I was obtained following the reported procedure⁵². L-*PrI and D-*PrI were synthesized and characterized as reported in **Supplementary Methods 2**.

Other reagents – D- and L-Proline Methyl Ester Hydrochloride (L-Pro-OMe HCl, purity 98 %), and cyclopentadienyl)cobalt(II) (CoCp₂, MQ100) were purchased from Aldrich. Iodomethane

(MeI, purity 99%) was purchased from Merck. Iodine (I₂) was purchased at vwr (purity: 99.5 %). All the reagents were used without any further purification.

Solvents – Methanol (anhydrous, purity 99.8%), N-N-Dimethylformamide (DMF, purity ≥ 99.8 %), Dimethyl sulfoxide (DMSO, purity ≥ 99.9 %), Propylene carbonate (PC, anhydrous, purity 99.7%), benzene (anhydrous, purity 99.8 %) were purchased at Sigma-Aldrich. Acetonitrile (ACN, anhydrous, purity 99.9 %, for electrolytes) was purchased at Scharlab. Ethyl acetate (99,5 %) and acetonitrile (HPLC grade, for CoCp₂I synthesis) were purchased at Fisher. All the solvents were used without any further purification.

Galvanic Intercalation: *Bulk crystals* – For intercalating bulk crystals, a rudimental two-electrode cell is employed. For intercalation with an In⁰ as the anode, a bulk crystal is clamped with Cu crocodile clip and used as a cathode (**Figure 2a**). When Zn⁰ or Mg⁰ are required, the bulk crystal is fixed to a platinum plate by means of In⁰ strips (see **Supplementary Figure 16**). Holding the crystals with In⁰ minimizes mechanical strain, and thus the probability of crystal cracks during intercalation. The crystal is electrically connected to the anodic metal of choice through a copper wire, previously sandpapered to remove the superficial native oxide or the polymeric coating and rinsed with iso-propanol. A source-measure unit operating as amperemeter (Keithley 2635) is placed in between the two electrodes to measure the galvanic discharge curve, i.e. the current flow versus time. This curve is useful to follow the intercalation process and capture the end of it.

The two electrodes are immersed in the electrolyte of choice. The intercalation starts spontaneously when the electrical circuit is closed, without the application of any external voltage. Usually, a complete bulk intercalation takes 1-2 days period time, depending on the mass of the bulk crystals (2-5 mg) and the intrinsic kinetic of the process. After intercalation the crystal is carefully disconnected from the circuit, rinsed thoroughly and left in a large volume of fresh MeOH or ACN for at least two hours. Then, the intercalated bulk crystal is placed in an oven at room temperature in a mild vacuum (~1 mbar) to accelerate the evaporation of the excess of solvent.

Multiple flakes – A bulk crystal is exfoliated using an adhesive tape (Nitto SPV224P) to obtain micro-sized and few-nm-thick flakes which are transferred on a thin film of Au(30 nm)/Ti(3 nm) film evaporated on glass. In the case of some vdW compounds (α -RuCl₃, VOCl, CrOCl, CrSBr), the Au substrates are exposed to 10-15 s of air-plasma before the transfer of the flake, using a Plasma Pen Atmospheric Plasma System (PVA TePla), to improve the transfer yield. In the case of intercalation using CoCp₂I, a Pt (30 nm)/Ti (3 nm) was used instead of Au, as Au is etched by the CoCp₂I solution.

Afterwards, the anodic metal is electrically connected to the Au film. In case of In⁰ as the anode, it is sufficient to cut an In⁰ piece and press it onto the surface of the substrate. In case of Zn⁰ or Mg⁰ as the anode, a piece of the metallic string is carefully sandpapered, cut in a ~ 25 mm² plate, and electrically connected to Au surface using In⁰ pieces and a copper wire, previously sandpapered and rinsed with iso-propanol (**Figure 3a**). The system is immersed in an Eppendorf microcentrifuge tube containing the desired electrolyte (**Figure 1e**) for a certain amount of time (between 20 min. and 1h 30 min.), which depends on the kinetic of the intercalation process. The optimized parameters for the successful intercalation of each vdW compound considered in this work are summarized in **Supplementary Table 1**. The substrate is finally rinsed with MeOH or ACN to remove the excess of the electrolyte.

Single flakes – Flakes are mechanically exfoliated from a bulk crystal using an adhesive tape (Nitto SPV224P) and transferred onto a Polydimethylsiloxane elastomer (PDMS). Homogeneous flakes with a typical thickness of 15-20 nm are selected and transferred onto prepatterned Au(15)/Ti(5) electrodes using a home-made delamination-stamping system. A piece of In⁰ is pressed onto the pad of one contact or, in case of Zn⁰ or Mg⁰ as the anode, a fragment of this metal is cut and pressed onto the In⁰ piece, which provides mechanical and electrical contact with the Au electrodes and the flake. Next, the electrochemical circuit is closed immersing the device in the electrolyte solution or, alternatively, by covering the device with a drop of the electrolyte solution. The intercalation time varies based on the kinetic of the intercalation for each host-guest combination and anodic metal. Typically, flakes are intercalated within seconds, in a molecular

diffusion limited regime of the intercalation kinetic. In some cases, the flakes detaches from the Au contact during intercalation, causing the interruption of the process. Finally, the device is finally rinsed with MeOH or ACN and dried naturally in air as for the “multi-flake” sample.

X-ray Diffractometry (XRD): XRD measurements were carried out using a Empyrean diffractometer (PANalytical) on bulk crystals and on exfoliated flakes supported on a Au(30-50)/Ti(3)/SiO₂ substrate. A copper cathode was used as X-ray source. Both the wavelengths $K\alpha_1$ (1.5406 Å) and $K\alpha_2$ (1.5443 Å) were employed to maximize the intensity of the diffracted beam.

Micro-Raman spectroscopy: Raman spectroscopy measurements of pristine and intercalated 2H-TaS₂ flakes were performed under ambient conditions with a Renishaw inVia Qontor equipped with a Nikon 100× objective (NA = 0.85) and a diffraction grating of 2400 lines mm⁻¹. A 532 nm laser was used with a power of ~ 1.7 mW for pristine and ~ 0.3 mW for the intercalated phase (~ 0.1 mW for few-layers flakes). Integration time was adjusted to enhance signal-to-noise ratio. In this case of the intensity maps of the TMA⁺ intercalated 2H-TaS₂ device (see **Supplementary Figure 15**) and TEA⁺ partially intercalated 2H-TaS₂ flake (see **Figure 3e**) the 532 nm laser power was set at ~ 1.7 mW and each spectrum was collected with an integration time of 15 s. Measurements were separated by 0.5 μm spacing.

Vibrating sample magnetometry (VSM): Magnetization vs. temperature or field H measurements were carried out using a physical properties measurement system (PPMS, Quantum Design) in vibrating sample magnetometer (VSM) mode.

Electrical transport measurements: The electrical measurements are recorded using a physical property measurement system (PPMS, Quantum Design) down to a temperature of 1.9 K. The resistance of pristine and intercalated flakes of 2H-TaS₂ and 2H-NbSe₂ are recorded via a four-points measurements, using a Keithley 6221 as a current source and a Keithley 2182 as a nanovoltmeter, operated in delta mode.

X-ray photoemission spectroscopy (XPS): First, pristine α -RuCl₃ and CoCp₂⁺ intercalated α -RuCl₃ bulk crystals were exfoliated under ultra-high vacuum (UHV) conditions ($p \leq 10^{-8}$ mbar).

XPS was carried out holding the sample at room temperature and illuminating it with monochromatized Al K α light ($h\nu = 1486.6$ eV) from a microfocus setup (SPECS Focus 600). The excited photoelectrons were collected by a SPECS 150 hemispherical analyzer at emission and incidence angles of 40° and 60°, respectively. The overall experimental resolution was extracted from Fermi edge analysis of a reference Au sample and resulted in 0.4 eV. The Fermi level position of the reference sample was subtracted to get core level emission in binding energy.

X-ray fluorescence: The analyses were conducted with a wavelength-dispersive X-ray fluorescence (WDXRF) spectrometer, model AXIOS from PANalytical, equipped with an Rh tube and three detectors (gas flow, scintillation, and sealed Xe). The solid sample (crystal) was placed in a Mylar sample holder in vacuum. The semi-quantitative software used is based on a series of scans with different analysing crystals to determine the presence of various elements. The semi-quantitative evaluation is carried out using the Fundamental Parameters method and the instrument's calibration, determined by the software based on a small set of standard samples associated with the software. Appropriate corrections were applied due to the sample's presentation (solid) and the use of the Mylar support. The results are normalized to 100%, accounting for the detected elements.

Acknowledgement

This work was supported under Projects PID2021-128004NB-C21 and PID2021-122511OB-I00 funded by Spanish MCIN/AEI/10.13039/501100011033 and by ERDF A way of making Europe; and under the María de Maeztu Units of Excellence Programme (Grant CEX2020-001038-M). This work was also supported by the FLAG-ERA grant MULTISPIN, via the Spanish MCIN/AEI with grant number PCI2021-122038-2A. B. M.-G. and M. G. acknowledge support from the “Ramón y Cajal” Programme by the Spanish MCIN/AEI (grant no. RYC2021-034836-I and RYC2021-031705-I).

Z.S. was supported by ERC-CZ program (project LL2101) from Ministry of Education Youth and Sports (MEYS) by the project Advanced Functional Nanorobots (reg. No.

CZ.02.1.01/0.0/0.0/15_003/0000444 financed by the ERDF). V.M. was supported by project LUAUS23049 from Ministry of Education Youth and Sports (MEYS). Dr. Iván Rivilla thanks Ikerbasque and acknowledges support from Grant PID2023-151549NB-I00 and RED2022-134287-T, funded by MICIU/AEI/10.13039/501100011033 and FEDER, EU, as well as Grant IT-1553-22 funded by the Basque Government. M.O. acknowledges the support from the UPV/EHU research project (EHU-N23/52).

A.M.-A. acknowledges support from the Basque Science Foundation for Science (Ikerbasque), POLYMAT, the University of the Basque Country, Diputación de Guipúzcoa, Gobierno Vasco (PIBA_2024_1_0030 and BERC programme) and Gobierno de España (Projects PID2021-124484OB-I00, CEX2020-001067-M and María de Maeztu Excellence Unit CEX2023-001303-M funded by MCIN/AEI/10.13039/501100011033). This project has received funding from the European Research Council (ERC) under the European Union's Horizon 2020 Research and Innovation Programme (Grant Agreement No. 722951). This work was funded by the European Union under the Horizon Europe grant 101046231. Project (PCI2022-132921) funded by the Agencia Estatal de Investigación through the PCI 2022 and M-ERA.NET 2021 calls.

The authors thank for technical and human support provided by Servicio General (SGIker) de Rayos X: Unidad de Rocas y Minerales (UPV/EHU).

Author information

Contributions D. T., M. O., M. G. conceived the study. D. T. and C. A. performed intercalations (bulk crystals and multi-flake) and the XRD measurements. D.T., C. A., D.M. and J. M. P. fabricated the devices for the intercalation of flakes and carried out the transport measurements. D. T. and B. M.-G. performed the Raman characterization. U. A., V. M. and Z. S. synthesized pristine bulk crystals of 2H-NbSe₂, 2H-TiS₂, 2H-SnS₂, FeOCl, VOCl, CrOCl, α -RuCl₃. Y. K. M., A. M-A. synthesized CoCp₂I. S. M.-V., E. C. synthesized pristine bulk crystals of CrSBr. F. M. S. and M. O. carried out the X-ray photoemission spectroscopy characterization. I. R. synthesized L- and D-*PrI. M. G., M.

O., F. C. and L. E. H. supervised the work. D. T. and M. G. wrote the manuscript, with inputs from all co-authors.

Corresponding authors

Correspondence to Marco Gobbi

Ethics declarations

Competing interests – The authors declare no competing interests.

Supplementary information

Supplementary Methods 1 – 2, Figs. 1–16, Tables 1–2.